CHAPTER 3. EXAMPLE OF A VISUALIZATION TECHNIQUE

In Chapter 2, we developed a visualization capability that can be used to analyze large sets of data. In this chapter, we will provide an illustrative example of these concepts using a finite-difference time-domain (FDTD) model of a rectangular microstrip patch antenna. Near-field quantities of the antenna will be visualized and compared to the theory of operation. We selected a microstrip patch antenna because it is explained analytically and is well documented in the literature.

Microstrip patch antennas are low-profile radiators that are typically lightweight, small in size, and conformable to planar and non-planar surfaces. Since patch elements are fabricated using printed-circuit technology, they can be manufactured in large quantities to reduce cost and are compatible with monolithic microwave integrated circuit (MMIC) designs. These antennas are well suited to applications where an aerodynamic profile and reliable performance are significant constraints. As a result, patch antennas have found numerous applications in aircraft, spacecraft, satellites and missiles [13].

The geometry and theory of operation of a rectangular microstrip antenna are explained in Sections 3.1 and 3.2, respectively. The geometry of the FDTD computational model is presented in Section 3.3, with primary focus placed on how the significant features of the microstrip patch antenna are modeled. Finally, the data is visualized in Section 3.4 and compared to the theory presented for the microstrip patch antenna. This comparison will demonstrate that radiation mechanisms can be identified visually.

3.1 Geometry of a Rectangular Microstrip Patch Antenna

The radiating patch of a microstrip antenna can be shaped in a variety of configurations including rectangular, circular, elliptical and triangular. The example presented in this chapter deals with a rectangular patch antenna. Figure 3-1 depicts the geometry of a rectangular microstrip patch antenna.
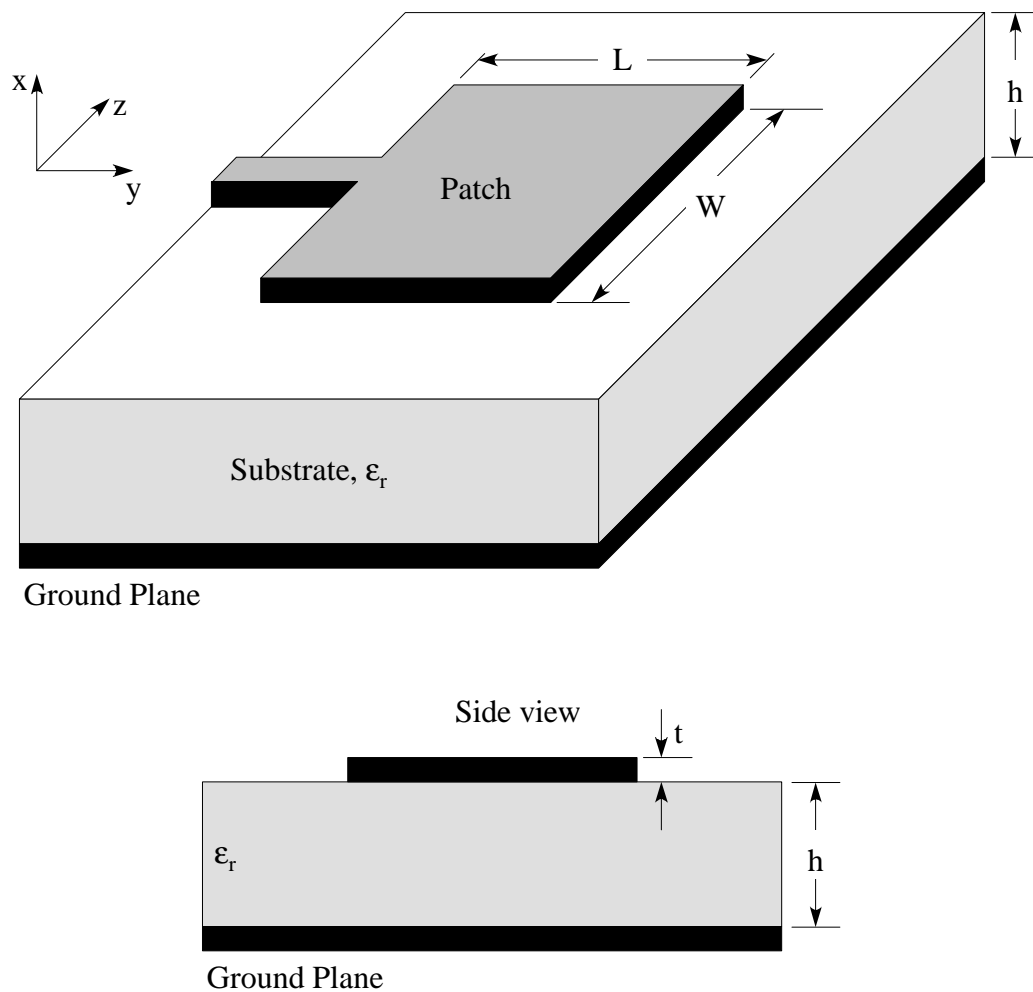
Figure 3-1. Geometry of a rectangular microstrip patch antenna (not to scale).

It is seen that a microstrip antenna is made up of a metallic patch and feed line that are offset from a ground plane by a dielectric substrate material. In order to eliminate the occurrence of surface waves, the thickness of the dielectric substrate is usually kept to a small fraction of a wavelength ($0.003\lambda_0 \leq h \leq 0.05\lambda_0$). Surface waves degrade the performance of a microstrip antenna in two ways. First, they reduce the total power that is available for direct radiation, which reduces the efficiency of the antenna. Second, surface waves adversely affect the pattern and polarization characteristics of the antenna since they are scattered at surface discontinuities, namely at the edges of the substrate and ground plane. The dielectric constant of the substrate usually falls in the range of $2.2 \leq \varepsilon_r \leq 12$. This is indicative of the trade-off that exists between antenna efficiency and element size. Substrate materials with lower dielectric constants are typically low loss, which results in higher antenna efficiency. Substrates with higher dielectric constants allow size reduction of the element at the expense of antenna efficiency (due to increased losses) [13].

Photo etching is commonly used to deposit the patch and feed line on the substrate, so the thickness of the metallization is very small ($t \ll \lambda_0$ where λ_0 is a wavelength in free space). The length of the metallic patch, L, is selected so that the antenna resonates at a particular operating frequency ($\lambda_0/3 \leq L \leq \lambda_0/2$). As we shall see in the next section, the length of the metallic patch needs to be tuned to account for the fringing fields at the edges of the patch. Finally, the width of the patch, W, is used to adjust the input impedance of the antenna [13].
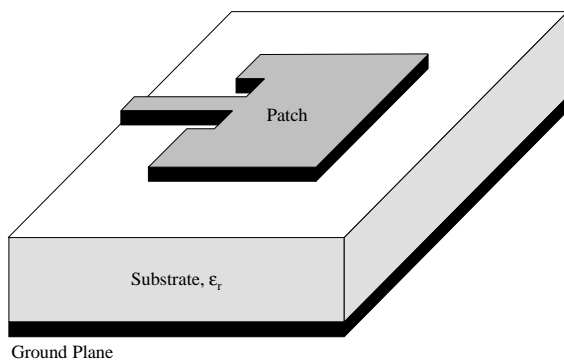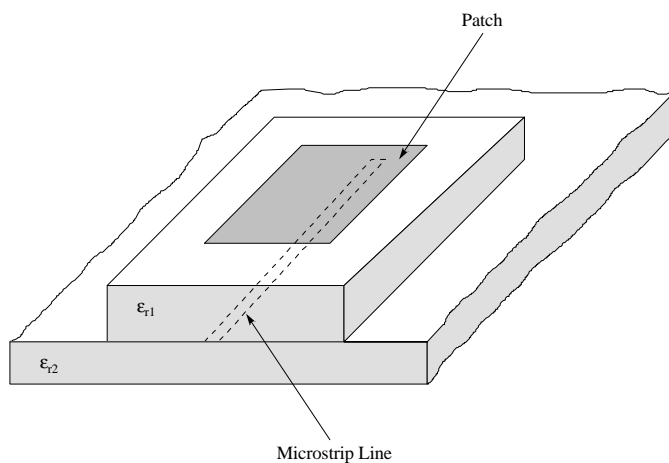
(a) Offset microstrip line feed
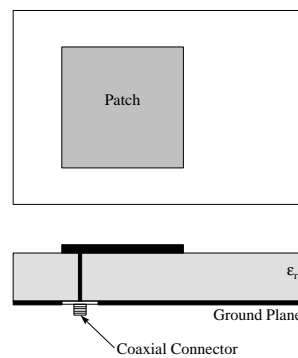
(b) Probe feed
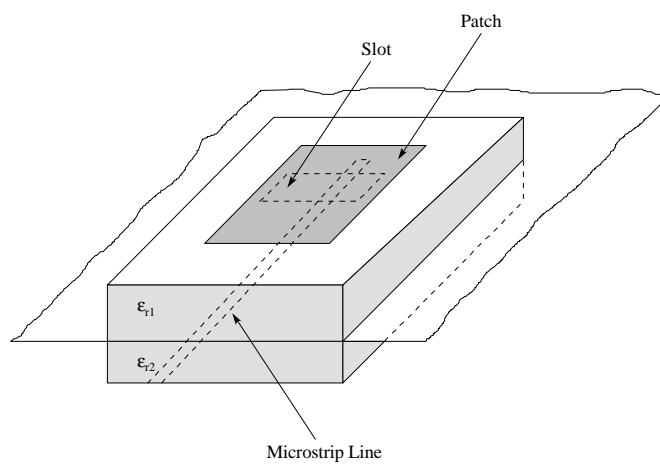
(c) Aperture-coupled feed

(d) Proximity-coupled feed

Figure 3-2. Feed configurations for microstrip antennas [13].

The patch element shown in Figure 3-1 uses a microstrip line feed. This is one of a number of feed arrangements that can be used with microstrip antennas. Figure 3-2 illustrates some of the more popular feed arrangements. The offset microstrip line feed eases the task of matching since the offset depth controls the input impedance of the antenna. Additionally, this configuration is simple to fabricate and lends itself well to analytical modeling. However, the feed line radiates and causes pattern and polarization degradation. The coaxial feed reduces spurious feed radiation and is easy to construct and match, although it tends to have a narrow bandwidth and is difficult to model analytically. The aperture-coupled feed isolates the feed mechanism from the radiating element through the use of a ground plane. Energy from the feed line is coupled to the element patch through the aperture slot. Unfortunately, the ground plane makes this feed configuration quite difficult to manufacture. Finally, the proximity-coupled feed removes the ground plane so it is easier to manufacture than the aperture-coupled feed. It has low spurious radiation, is fairly easy to analyze, and provides the largest bandwidth of the feed configurations presented here [13].

In this section we have defined the geometry of a rectangular microstrip patch antenna. Now we are prepared to discuss the analytical methods used to model and characterize the antenna. In the next section, three techniques will be reviewed: the transmission-line method, the cavity model, and numerical techniques. Then, in Section 3.3 we will model a microstrip patch antenna using a FDTD computational code.

3.2 Theory of Operation

Microstrip patch antennas have been analyzed using a variety of techniques. Three well-known methods are the transmission-line model, the cavity model, and full-wave numerical models. Below we will provide an overview of each of the three methods and discuss the strengths and weaknesses of each.

3.2.1 Transmission Line Model

The transmission-line model is the simplest of the three techniques we will consider and, as a result, is the least accurate. The microstrip antenna is modeled as two radiating slots that are separated by a distance L_{eff}. Referring to Figure 3-3, we can see the physical meaning of L_{eff}. It is essentially the length of the patch, L, plus an additional distance, $2\Delta L$, to account for the fact that the patch looks electrically wider due to the fringing fields. Balanis [13] provides the following formula for the added distance

$$\Delta L = 0.412 h \frac{\left(e_{reff} + 0.3\right)\left(\dfrac{W}{h} + 0.264\right)}{\left(e_{reff} - 0.258\right)\left(\dfrac{W}{h} + 0.8\right)}. \tag{3-1}$$

In the above equation, ε_{reff} is the effective dielectric constant of a microstrip transmission line given by [8]

$$e_{reff} = \frac{e_r + 1}{2} + \frac{e_r - 1}{2}\left(1 + 12\frac{h}{W}\right)^{-1/2}. \tag{3-2}$$

Thus, the effective distance separating the two radiating slots becomes

$$L_{eff} = L + 2\Delta L. \tag{3-3}$$

Finally, Balanis [13] uses this adjusted length to calculate the resonant frequency of the antenna

$$(f_r)_{010} = \frac{c}{2 L_{eff} \sqrt{e_{reff}}} , \tag{3-4}$$

where c is the speed of light in a vacuum.

Since the transmission-line model accounts for the fringing effects at the edges of the patch, it provides a good characterization of the resonant frequency. It also models the input impedance of the antenna fairly accurately. However, it does not account for the affects of a truncated dielectric substrate or a finite ground plane nor does it provide insight into the radiation patterns of the antenna. Additionally, the model breaks down as the height of the dielectric substrate, h, becomes a significant portion of a wavelength.
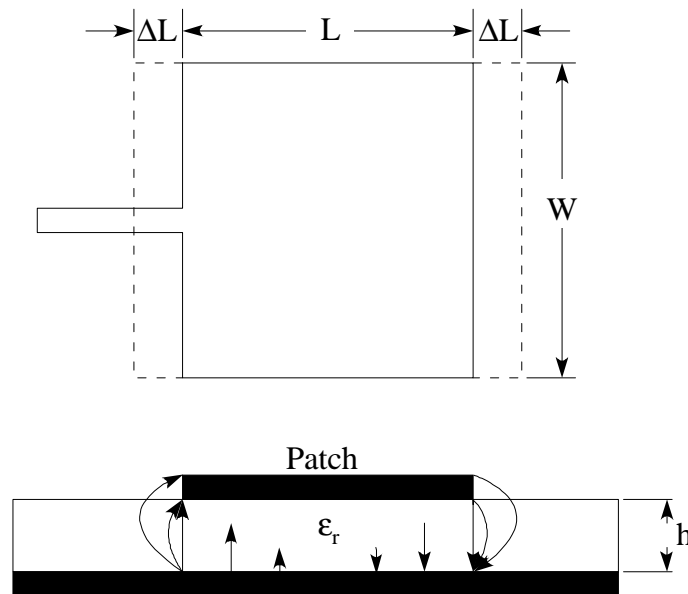
Figure 3-3. Transmission-line model of microstrip antenna [13].

3.2.2 Cavity Model

In order to gain insight into the radiating mechanism of an antenna, we need to first understand the near-field quantities that are present on the structure. The cavity model aids in this pursuit since it provides a mathematical solution for the electric and magnetic fields of a microstrip antenna. It does so by using a dielectrically loaded cavity to represent the antenna. As we can see in Figure 3-4, this technique models the substrate material, but it assumes that the material is truncated at the edges of the patch. The patch and ground plane are represented with perfect electric conductors and the edges of the substrate are modeled with perfectly conducting magnetic walls. It should be noted that the cavity model does not include feed effects; the feed is shown in the figure simply for reference.
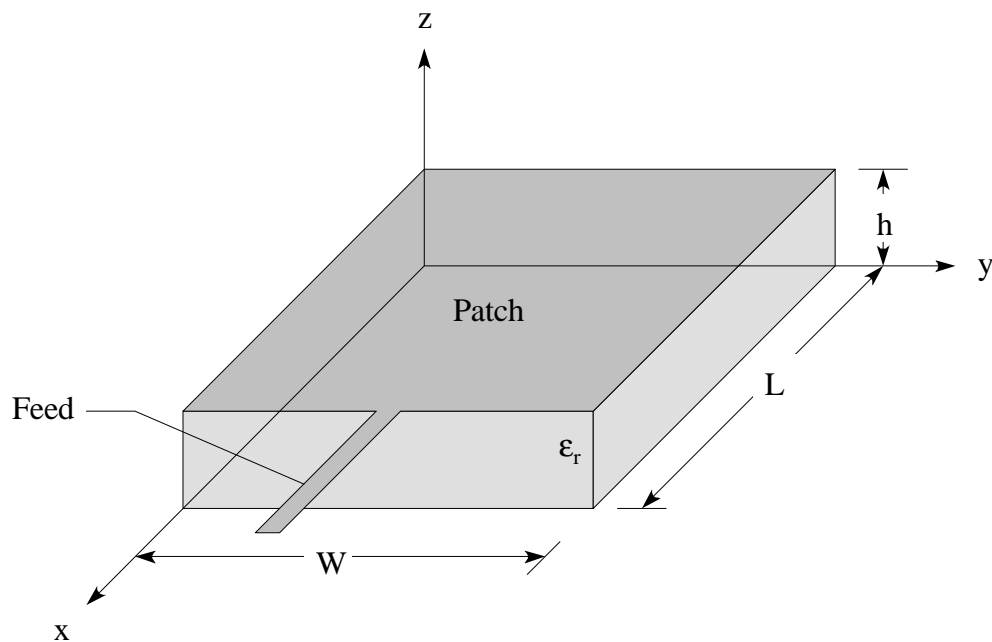

Figure 3-4. Geometry of cavity model.

Balanis formulates a solution to the above cavity problem using the vector potential approach [8] and [13]. Summarizing the technique, we begin by assuming that the dielectric is very thin, which means that the electric field is constant along the height of the substrate, h, and is nearly normal to the surface of the patch. Therefore, we only need to consider TM$_z$ modes inside the cavity. Now, we can write an expression for the electric and magnetic fields within the cavity in terms of the vector potential A$_z$ [8]:

$$E_x = -j\frac{1}{\omega\mu\epsilon}\frac{\partial^2 A_z}{\partial x \partial z} \qquad\qquad H_x = \frac{1}{\mu}\frac{\partial A_z}{\partial y}$$

$$E_y = -j\frac{1}{\omega\mu\epsilon}\frac{\partial^2 A_z}{\partial y \partial z} \qquad\qquad H_y = \frac{1}{\mu}\frac{\partial A_z}{\partial x} \ . \qquad (3\text{-}5)$$

$$E_z = -j\frac{1}{\omega\mu\epsilon}\left(\frac{\partial^2}{\partial z^2} + k^2\right)A_z \qquad\qquad H_z = 0$$

Since the vector potential must satisfy the homogeneous wave equation

$$\nabla^2 A_z + k^2 A_z = 0 , \qquad (3\text{-}6)$$

we can use separation of variables to write the following general solution

$$A_z = \left[A_1\cos(k_x x) + B_1\sin(k_x x)\right]\left[A_2\cos(k_y y) + B_2\sin(k_y y)\right]$$
$$\cdot\left[A_3\cos(k_z z) + B_3\sin(k_z z)\right] \qquad (3\text{-}7)$$

where k$_x$, k$_y$, and k$_z$ are wavenumbers. Applying the boundary conditions

$$
\begin{aligned}
E_x = 0 \quad &for \quad 0 \le x \le L, 0 \le y \le W, z = 0 \\
&and \quad 0 \le x \le L, 0 \le y \le W, z = h \\
H_x = 0 \quad &for \quad 0 \le x \le L, y = 0, 0 \le z \le h \\
&and \quad 0 \le x \le L, y = W, 0 \le z \le h \\
H_y = 0 \quad &for \quad x = 0, 0 \le y \le W, 0 \le z \le h \\
&and \quad x = L, 0 \le y \le W, 0 \le z \le h
\end{aligned}
\qquad (3\text{-}8)
$$

we obtain a solution for the electric and magnetic fields inside the cavity:

$$E_x = -j\frac{k_x k_z}{wme} A_{mnp} \sin(k_x x)\cos(k_y y)\sin(k_z z)$$

$$E_y = -j\frac{k_y k_z}{wme} A_{mnp} \cos(k_x x)\sin(k_y y)\sin(k_z z)$$

$$E_z = -j\frac{(k^2 - k_z^2)}{wme} A_{mnp} \cos(k_x x)\cos(k_y y)\cos(k_z z)$$ (3-9)

$$H_x = -\frac{k_y}{m} A_{mnp} \cos(k_x x)\sin(k_y y)\cos(k_z z)$$

$$H_y = \frac{k_x}{m} A_{mnp} \sin(k_x x)\cos(k_y y)\cos(k_z z)$$

$$H_z = 0$$

Here,

$$\left.\begin{array}{ll} k_x = \dfrac{mp}{L}, & m = 0, 1, 2, \ldots \\[2mm] k_y = \dfrac{np}{W}, & n = 0, 1, 2, \ldots \\[2mm] k_z = \dfrac{pp}{h}, & p = 0, 1, 2, \ldots \end{array}\right\} \quad m = n = p \neq 0$$ (3-10)

and A_{mnp} is the amplitude coefficient. Finally, the resonant frequencies for the cavity are given by

$$(f_r)_{mnp} = \frac{1}{2p\sqrt{me}}\sqrt{\left(\frac{mp}{L}\right)^2 + \left(\frac{np}{W}\right)^2 + \left(\frac{pp}{h}\right)^2}.$$ (3-11)

Examining the above fields for $(TM_z)_{100}$ dominant mode excitation, we see that $k_y = k_z = 0$ and the field components reduce to

$$E_z = -jwA_{100}\cos\left(\frac{p}{L}x\right)$$
$$H_y = \frac{p}{mL}A_{100}\sin\left(\frac{p}{L}x\right)$$ (3-12)

We can convert to equivalent electric and magnetic current densities using:

$$\vec{J} = \hat{n} \times \vec{H}$$
$$\vec{M} = -\hat{n} \times \vec{E}$$

(3-13)

where $\hat{n}$ is the outward directed surface normal. The magnetic field is zero along the

x=0 and x=L walls and is normal to the surface along the y=0 and y=W walls. Therefore,

no equivalent electric current density flows on the walls of the cavity. The electric field

results in a non-zero magnetic current density on the walls of the cavity. Figure 3-5

shows both the electric field and corresponding magnetic current densities for the

microstrip antenna. The magnetic currents can be broken into a pair of radiating slots and

a pair of non-radiating slots. The radiating slots are in phase so they will constructively

interfere in the far-field. Thus, these two slots form the primary radiating mechanism for

the microstrip antenna. On the other hand, the non-radiating slots are out of phase so

they will destructively interfere in the far-field and will not contribute to the radiated
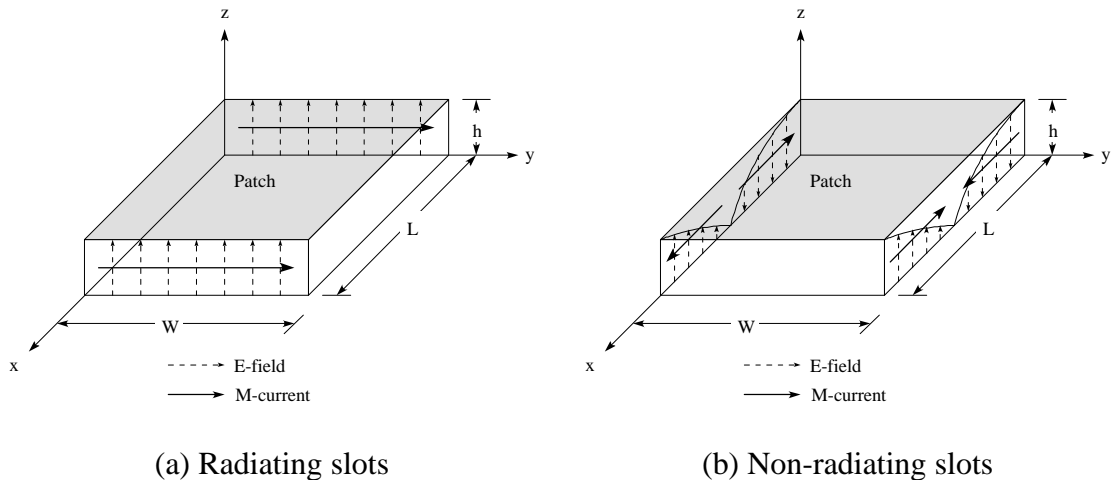
fields.

(a) Radiating slots   (b) Non-radiating slots

Figure 3-5. Field configurations and current densities for microstrip patch [13].

33

From the above results, we can see that the cavity model provides excellent insight into the radiating mechanism of a microstrip patch antenna. It provides the field configurations of the radiating and non-radiating slots that can be used to solve for the radiation patterns [13]. Since the antenna is modeled as a cavity, additional work is necessary to accurately model the input impedance. An effective loss tangent needs to be added to account for the power that is lost to radiation [13]. Alternatively, the radiated energy can be modeled using an impedance boundary condition at the walls [14].

Although the cavity model is quite adept at modeling the radiating mechanism for a microstrip antenna, it does have some limitations. First, the cavity model does not model the feed effects. Nor does it model the adverse effects introduced by a finite substrate and ground plane. One way to circumvent these limitations is to employ numerical techniques.

3.2.3 Full-Wave Numerical Models

In some instances, we may need to understand how the behavior of an antenna is affected by its surroundings. For example, we may want to develop a model that includes the effects of a feed structure, a finite ground plane, or a case enclosure. For problems such as these, the techniques described above become highly impractical. Fortunately, there are a variety of numerical analysis techniques that can handle these problems quite nicely, including the method of moments (MoM), the finite-element method (FEM), and the FDTD method. All three of these techniques are computationally intensive, which in the past limited the size and complexity of problems that could be approached. However, due to recent advances in computing capabilities, these techniques have become much

34

more powerful. In addition, these techniques are somewhat generalized so they are capable of modeling a variety of antennas (not just the microstrip patch). The details of each technique are quite intricate, so we will focus on the FDTD method because it is used to generate the examples presented in this thesis.

The FDTD method uses a discretization in time and space to calculate a solution of Maxwell's curl equations directly in the time domain [15]:

$$\nabla \times \vec{E} = -m\frac{\partial \vec{H}}{\partial t}$$
$$\nabla \times \vec{H} = e\frac{\partial \vec{E}}{\partial t} + \vec{J}$$

(3-14)

Rearranging these equations, with $\vec{J} = s\vec{E}$, we obtain

$$\frac{\partial \vec{H}}{\partial t} = -\frac{1}{m}\nabla \times \vec{E}$$
$$\frac{\partial \vec{E}}{\partial t} = \frac{1}{e}\nabla \times \vec{H} - \frac{s}{e}\vec{E}$$

(3-15)

Evaluating the vector curl operator ($\nabla \times \vec{A}$) and employing central differencing in both time and space to approximate the partial derivatives, we obtain six update equations (one for each component of the electric and magnetic fields). For example, the update equation for the E_x component is as follows:

$$E_x^n(i,j,k) = \left[\frac{e}{e + s\Delta t}\right]E_x^{n-1}(i,j,k) + \left[\frac{\Delta t}{e + s\Delta t}\right]$$
$$\cdot\left[\begin{array}{c} \dfrac{H_z^{n-1/2}(i,j,k) - H_z^{n-1/2}(i,j-1,k)}{\Delta y} \\ -\dfrac{H_y^{n-1/2}(i,j,k) - H_y^{n-1/2}(i,j,k-1)}{\Delta z} \end{array}\right].$$

(3-16)

The electromagnetic structure is modeled by approximating its geometry and composition with Yee cells of different material parameters (both conductivity and relative dielectric constant). Figure 3-6 depicts an example Yee cell along with its corresponding field calculation points. At the outer boundaries of the computational space an absorbing boundary condition is used to simulate free-space radiation. In order to avoid numerical instabilities in the finite-difference algorithm, the time increment must not violate the Courant stability condition [4]:

$$\Delta t \leq \frac{\left(me\right)^{1/2}}{\left[\dfrac{1}{\Delta x^2} + \dfrac{1}{\Delta y^2} + \dfrac{1}{\Delta z^2}\right]^{1/2}} . \qquad (3\text{-}17)$$

An excitation is then applied to the computational model and the $\vec{E}$- and $\vec{H}$-field computations are alternately marched through time from time zero to the desired stopping point. Results can be viewed either in the time domain or in the frequency domain. In order to obtain the frequency characteristics of the antenna it is necessary to compute a fast-Fourier transform (FFT) of the transient output data.

The FDTD techniques presented above allow antennas to be modeled in fine detail. Feed lines, finite ground planes, and case enclosures can all be included in the computational model. In addition, the techniques are highly generalized so a number of antennas can be analyzed. Tirkas and Balanis [4] demonstrate the versatility of FDTD techniques by using it to model a dipole, open-ended waveguide, and horn antenna. The major drawback of numerical techniques in general is that they generate huge amounts of data. However, we can alleviate this problem greatly through the use of visualization.
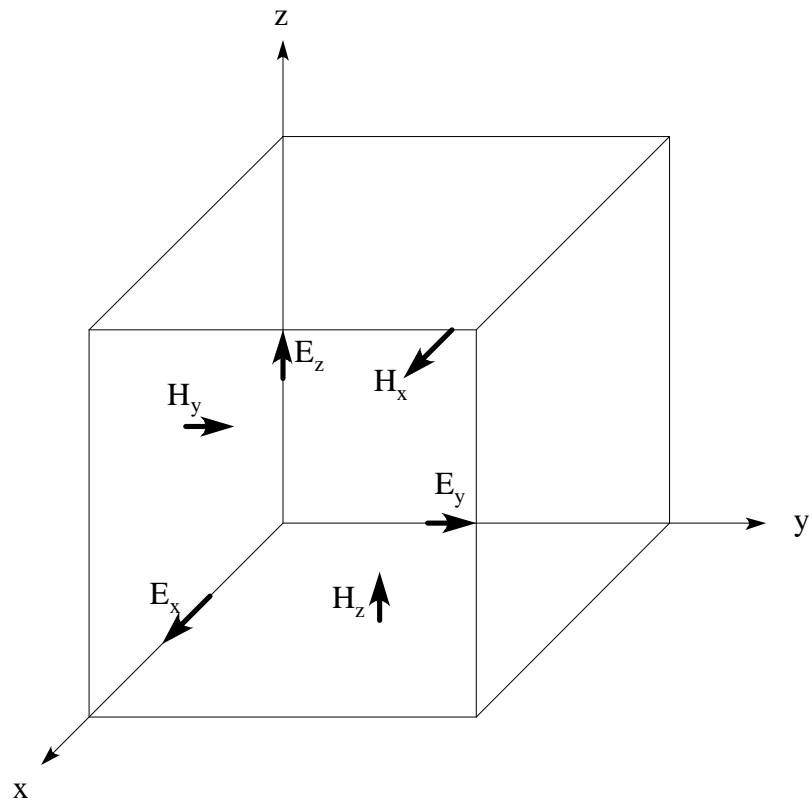
Figure 3-6. Example Yee cell with field calculation points.

3.3 Geometry of Computational Model

In order to simulate an antenna using FDTD we first must model the geometry in the computational space. This is a tedious process since care needs to be taken so that all of the important details of the antenna are modeled properly. In many cases this can be an iterative process that involves correcting errors and determining how finely certain details need to be modeled. Figure 3-7 shows the layout of the FDTD computational space that was used to simulate the rectangular microstrip patch antenna.

y

44 cells

49 cells   29 cells   33 cells

3 cells

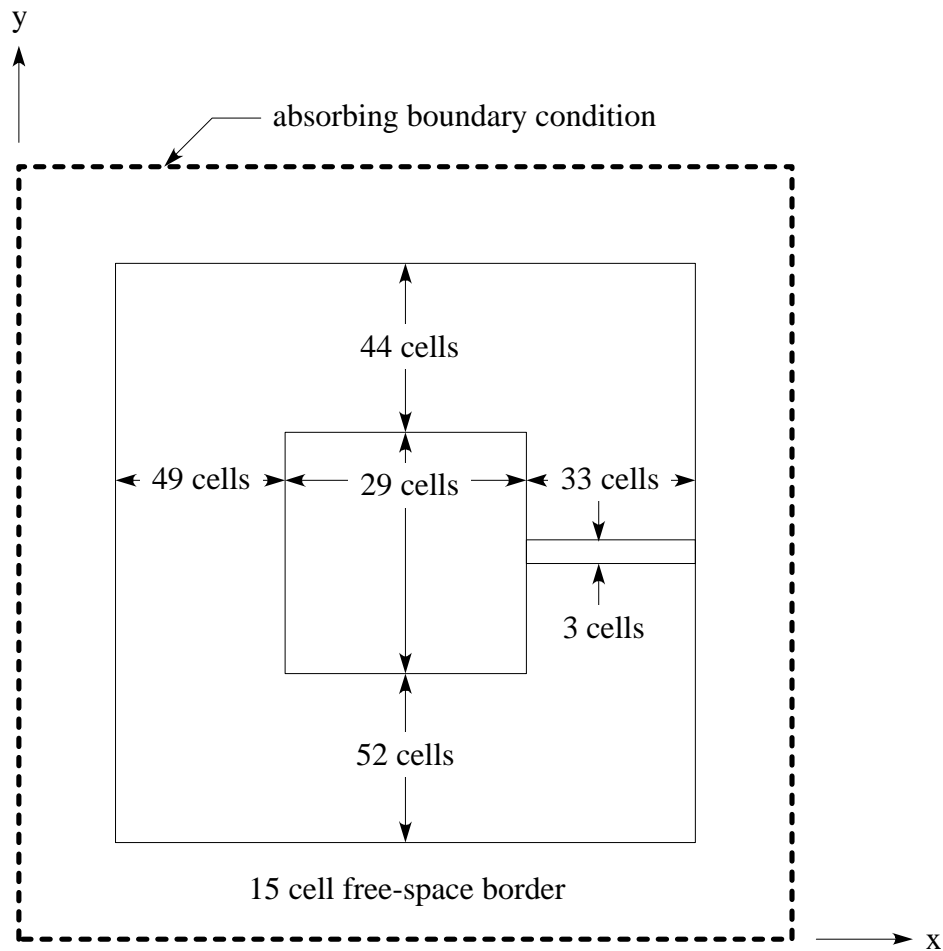52 cells

15 cell free-space border

x

Figure 3-7. FDTD computational space.

As we can see, the feed line and finite ground plane are included in the model. The microstrip line is fed at the edge of the substrate by a z-directed (out of the page) infinitesimal dipole, which simulates a microstrip to coaxial line connector. The dielectric substrate (Duroid 5870, ε_r=2.35) is modeled with three Yee cells in the z-dimension (out of the page). A free-space border is placed between the antenna and the absorbing boundary condition to avoid any instability that could be caused by coupling.

38

We elected to excite the antenna for dominant mode operation (f = 3 GHz). The FDTD computational engine was run on a Pentium 133 personal computer with 64 Megabytes of memory. The total execution time for this model was approximately 96 hours. In the next section we will present animations of the equivalent current densities located on a planar surface a single Yee cell above the metallization. This should allow us to view the radiating mechanism, the affect of the finite ground plane, and the affect of the feed line.

3.4 Application of Visualization Technique

This section will provide an example of the visualization techniques that were developed in Chapter 2. Results from the above FDTD model of a rectangular microstrip patch antenna will be visualized. The visualization techniques involve converting phasor data to a time domain animation so that magnitude and phase information is displayed concurrently; however, the vector components will be viewed separately. Figure 3-8 depicts the visualization network that was used in AVS to generate the animations. Essentially, the data is read in, colorized, displayed, and output to an image format. These images are then combined in Adobe Premiere to form the animations that are presented below.
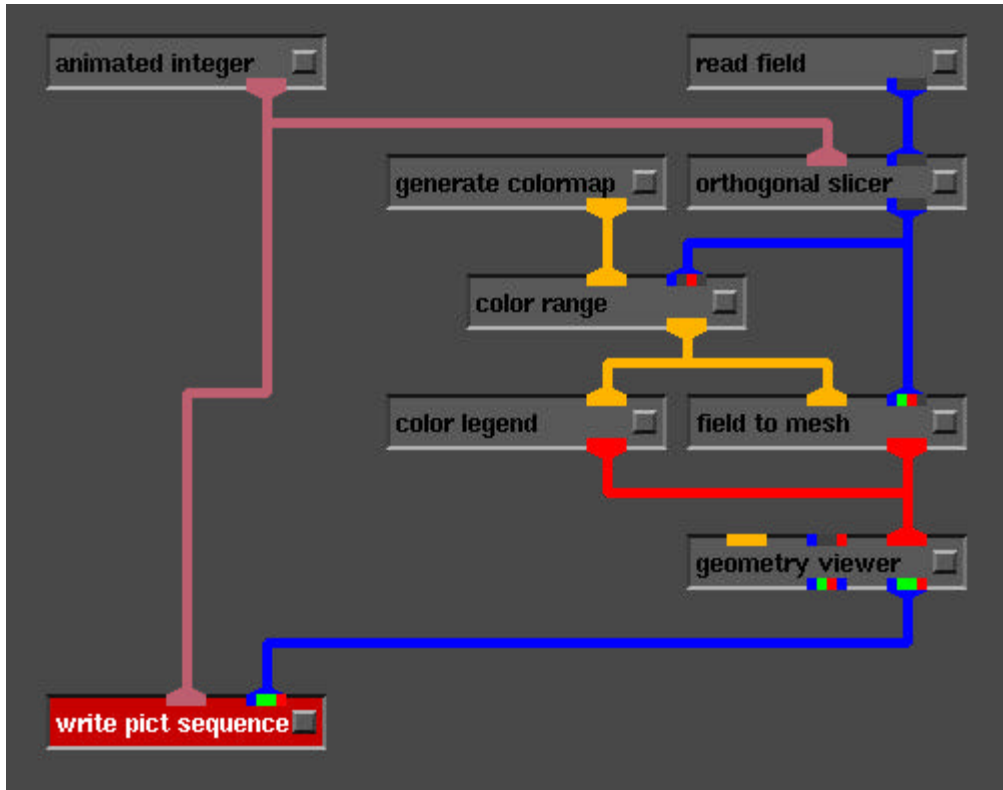
Figure 3-8. AVS visualization network used to generate examples.

Figures 3-9 to 3-12 contain the animations of the magnetic and electric equivalent current densities. Starting with the M_y component, which is shown in Figure 3-9, we can see that the FDTD results are quite inclusive. The radiating slots are present and behave as the cavity model predicted, although the patch edge that is connected to the feed has a slight asymmetry. We also see that the feed line is contributing a cross-polarization to the radiation pattern, which is the same order of magnitude as the primary radiating mechanism. This is important since cross-polarization is undesirable in many antenna applications. In addition, the effect of the finite ground plane is evident and is also the same amplitude as the radiating slots. This can have adverse effects on the radiation

40

pattern since a larger distance than the patch edges separates the edges of the ground plane. Now instead of having an array of two radiating slots, we have an array of four slots. This may lead to unwanted nulls in the antenna pattern. We also see two unexpected results. First, there appears to be a small amplitude surface wave that is propagating in the dielectric substrate. Also, we can see a backspill of the feed excitation. This is due to the fact that we used an infinitesimal dipole, which has an omnidirectional radiation pattern.

The M_x field component is displayed in Figure 3-10. From the color legend we can see that amplitude of this component is the same as the M_y component. This component includes the non-radiating slots that were predicted by the cavity model. These slots are out of phase and will cancel in the far field as the cavity model suggested. In addition we see a standing wave on the feed line that has a small traveling wave component; the latter is characteristic of a radiating structure. We also see the affects of the finite ground plane, although these quantities cancel in the far field so they do not adversely affect the radiation pattern.

Figures 3-11 and 3-12 show the J_x and J_y components, respectively. These quantities are much smaller in amplitude than the magnetic current densities, which was suggested by the cavity model (ideally they should be zero). In addition to the small amplitude of these components, they will cancel in the far field since they are out of phase. Therefore, they should have a negligible affect on the overall radiation pattern.
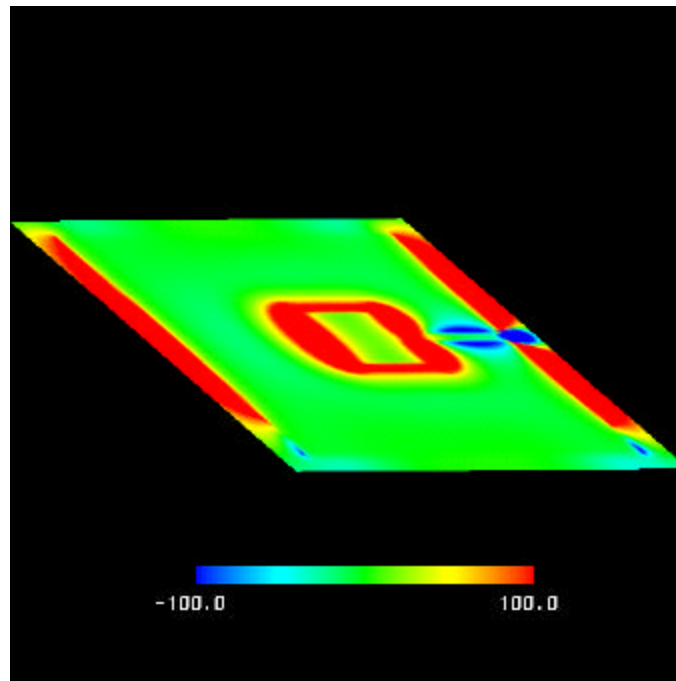
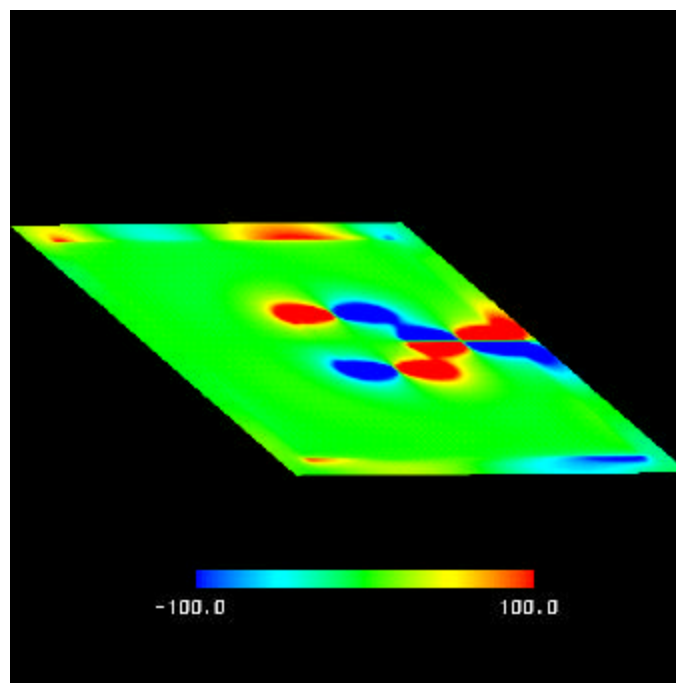Figure 3-9. M_y equivalent magnetic current density.

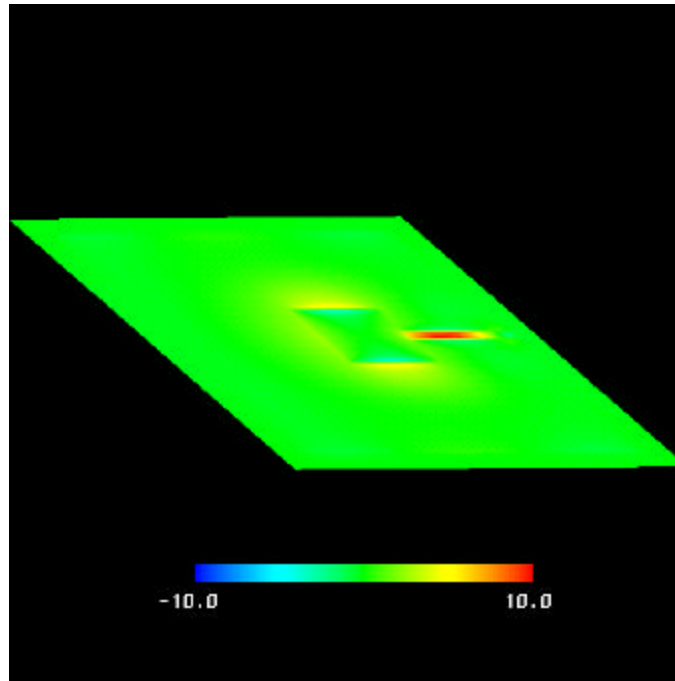Figure 3-10. M_x equivalent magnetic current density.
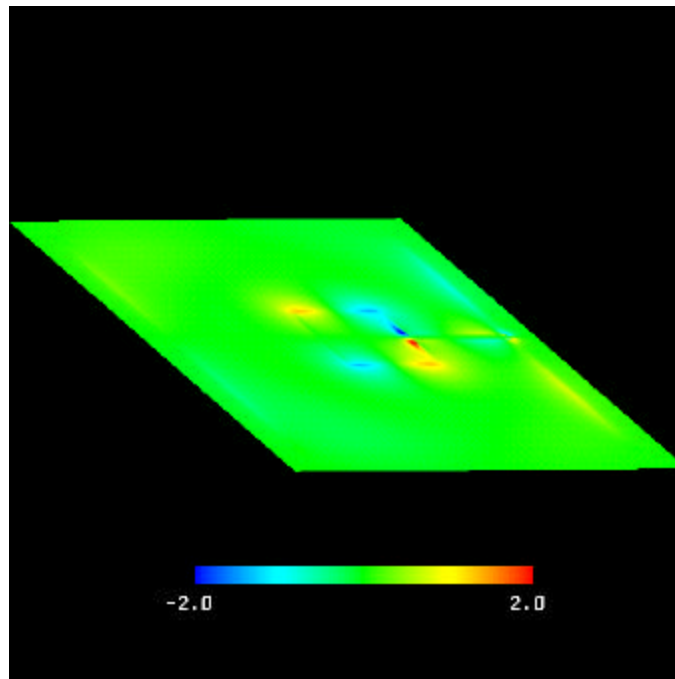
Figure 3-11. J_x equivalent electric current density.

Figure 3-12. J_y equivalent electric current density.